

Anisotropic Heterobimetallic Nanomaterials with Controlled Composition for Efficient Oxygen Reduction at Ultralow Loading

Siyi Ming, Samuel J. Cobb, Motiar Rahaman, Nicholas Sammy, Erwin Reisner, and Andrew E. H. Wheatley*

Hydrogen fuel cells represent a leading technology in developing green energy targeting net-zero emissions goals by mid-century. However, the sluggish kinetics of the oxygen reduction reaction (ORR) have hitherto demanded substantial quantities of expensive platinum (Pt) group metals. Advances in catalyst design, including the controllable fabrication of highly branched morphologies to increase the surface area-to-volume ratio, intermixing Pt with more affordable transition metals, and controlling composition, offer solutions that can further enhance activity and reduce expense. In this context, Pt/M (M = Fe, Ni, Co) nanopods and nanodendrites with precise composition control using more affordable starting materials are designed and crafted. The method is highly efficient, taking only 30 min and avoiding the need for high-pressure equipment, making it highly scalable. These catalysts show superior ORR performance at an electrode loading as low as $0.0022 \text{ mg}_{\text{Pt}} \text{ cm}^{-2}$. One, nanodendritic Pt/Ni, achieves a mass activity of $0.55 \text{ A mg}_{\text{Pt}}^{-1}$ at 0.9 V versus RHE, making it 87 times more efficient in terms of Pt-content than a commercial 10 wt% Pt/C nanoparticle standard. These findings provide new opportunities for developing next-generation, cost-efficient Pt-based catalysts, by potentially advancing hydrogen fuel cell technology through performance enhancement and addressing cost challenges through catalyst design.

cost of the fuel cell stack,^[1] combined with the energy security implications of depending on precious metals, have led to considerable efforts directed at minimizing Pt use through catalyst design approaches such as nanostructuring (e.g., nanoframes,^[2] nanocages^[3]) and the use of single-atom metal catalysts.^[4] These strategies aim to enhance the exposure of active sites and amplify performance in the oxygen reduction reaction (ORR), a critical step in HFC operation. Structure manipulation, metal intermixing, and targeting the surface expression of catalytically active facets have led to performance enhancement using Pt-based nanocrystals in acidic media.^[5] More recently, alkaline environments have been studied that are less corrosive and offer reduced anion adsorption and improved kinetics.^[6] However, problems have emerged with optimizing the oxygen binding strength of Pt in the presence of hydroxide.^[5] This background shows that different media have advantages and drawbacks and makes clear the potential power of an overarching

1. Introduction

Platinum (Pt) finds frequent use in hydrogen fuel cells (HFCs). However, the cost this incurs, accounting for 40%–50% of the

approach to catalyst design that offers electrocatalysts with controlled composition and shapes applicable to HFC technology irrespective of electrolyte environment. More widely, intricate, highly engineered catalysts currently tend to require expensive, multi-step and, for structures like nanodendrites, rather empirical syntheses.^[7]

To maximize the availability of surface active sites for minimal material cost, branched morphologies with high surface-area-to-volume ratios have attracted attention.^[8] Examples of these anisotropic nanoparticles (NPs) include nanopods – either individually or incorporated within more complex nanodumbbells^[9] – as well as nanodendrites, both of which demonstrate distinct branched shapes. These morphologies naturally develop under kinetic control, where the rate of atom deposition onto growing seeds exceeds that of their subsequent migration between facets, resulting in branched structures. This inherent growth characteristic offers the opportunity to use commercially available substrates for synthesis under facile conditions. It has therefore been the subject of work exploring the manipulation of various parameters,^[10] including temperature,^[11] reductant addition,^[12]

S. Ming, S. J. Cobb^[+], M. Rahaman, N. Sammy, E. Reisner, A. E. H. Wheatley
Yusuf Hamied Department of Chemistry
University of Cambridge
Lensfield Road, Cambridge CB2 1EW, UK
E-mail: aehw2@cam.ac.uk

 The ORCID identification number(s) for the author(s) of this article can be found under <https://doi.org/10.1002/adfm.202411006>

^[+]Present address: Department of Chemistry, The University of Manchester, Oxford Road, Manchester M13 9PL, UK

© 2024 The Author(s). Advanced Functional Materials published by Wiley-VCH GmbH. This is an open access article under the terms of the [Creative Commons Attribution](#) License, which permits use, distribution and reproduction in any medium, provided the original work is properly cited.

DOI: 10.1002/adfm.202411006

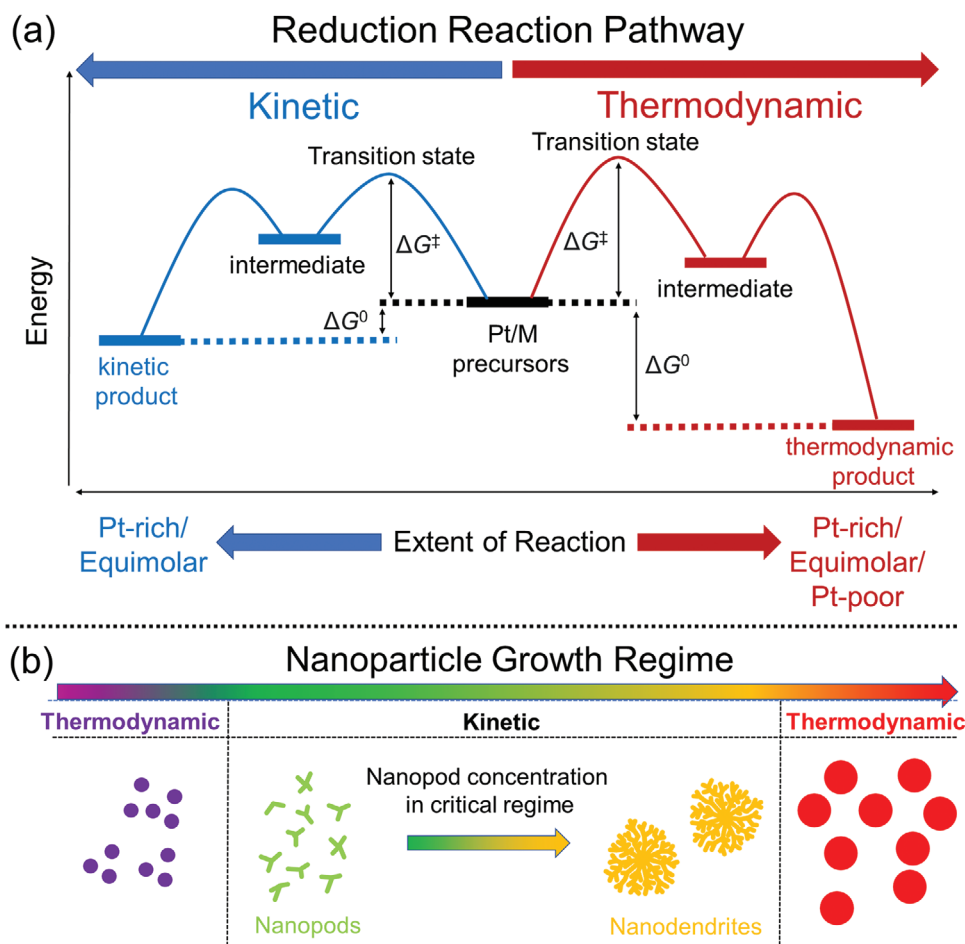


Figure 1. a) Influence on nanoparticle composition of reducing metal precursors under kinetic or thermodynamic control; b) Nanoparticle growth regimes as a function of feedstock supply under (left to right) more chemically reducing conditions.

and synthesis time.^[13] While this has previously aimed to guide NP growth toward the kinetic regime and facilitate nanopod production, it is only very recently that a similar exploration of nanodendrite formation has been attempted.^[14] This led to a recognition that achieving a critical concentration of nanopods underpinned the establishment of a collision-based mechanism in which the nanopod arms underwent branching to give more complex yet predictable morphologies.

Increasing the number of active sites and enhancing the intrinsic activity of those sites already represent key strategies in catalyst design.^[15] The ability of highly branched catalysts to display relatively high electrochemical surface areas^[16] and therefore to express more active sites is established.^[17] The same is true of the ability to enhance the intrinsic activity of a site by manipulating chemical composition to yield charge transfer effects.^[18] However, controllably achieving significant improvements in these areas is vastly challenging due to platinum's prominent position in the volcano plot of ORR activity against composition, as established by decades of experimental validation^[19] and backup by Density Functional Theory (DFT).^[20] Simulations have explained how manipulating surface facets to enhance expression of the ORR-active (111) plane^[21] and intermixing Pt with other metals and semimetals can 1) lower barriers to reaction,^[22] 2) modulate

adsorption energies of oxygen intermediates,^[23] 3) promote electron transport and the filling of active site orbitals,^[24] and 4) enhance kinetic stability.^[25] Maximizing ORR activity also requires precise control of catalyst composition.^[26] The main synthetic challenge to overcome in doing this is the positive reduction potential of Pt, which promotes the formation of Pt-rich or equimolar materials.^[9] Additionally, changes in composition typically require alterations in the reduction rates of the different metal ions. In turn, this impacts particle nucleation and growth rates, potentially inducing alterations in shape that may counteract any benefits of careful morphology design.^[15] Overall, the ability to *independently* manipulate morphology and composition promises access to a new generation of catalysts.

Manipulating both composition and morphology in Pt-based NPs relies on 2 key factors. First, the reaction pathway (chemical reduction in this work) should be directed into the thermodynamic regime. This eliminates the control of positive reduction potential on product composition and enables noble metal-poor compositions (Figure 1a).^[27] Second, modulating conditions (type and relative concentration of reagents, temperature, etc.) control NP shape by affecting nucleation and growth rates. The latter gives rise to different morphologies depending on whether growth is thermodynamic or kinetic (Figure 1b).^[10]

Near-pseudospherical thermodynamic growth results from a low flux of reduced metal monomers (in this case, atoms). If conditions are made more reducing, kinetic control and anisotropic nanopod formation are enforced because the evolution of high-energy facets outstrips the migration of adatoms to lower-energy facets or because nanocrystallites collide and exhibit oriented attachment.^[28] This switch is driven by the rapid evolution of high-energy facets due to increased feedstock availability. Further raising the reduction rate then gives more nucleation events, depletes the feedstock available for growth, and yields smaller anisotropic particles with truncated arms. Finally, very strongly reducing conditions cause a reversion to thermodynamic near-pseudospheres as growth proceeds rapidly on all facets.^[14] Crucially, by tuning reducing conditions even within the thermodynamic reduction regime, kinetic NP growth can be achieved, giving anisotropic products.

Recent work suggested that in the specific case of Pt/Fe anisotropy is achievable by fine-tuning the nucleation rate and hence the balance between seeds and reduced monomers available for growth.^[11] In that instance, a range of reduction rates at which nanodendrites formed emerged through the systematic variation of the reducing strength of the system. This was done by altering temperature, reagent dilution, and the relative amounts of oleic acid (OA) and oleylamine (OAm), establishing that nanodendrites occurred when the experimental variation of these parameters achieved the creation of a critical nanopod concentration. This resolved not only the challenge of creating nanodendrites predictably but also afforded a reliable route to highly branched nanoparticles *and* Pt-poor compositions in bimetallic Pt/Fe systems.^[14] For that system, dual control over morphology and composition came from achieving an understanding of the effects of adjusting individual synthetic parameters and so being able to make multiple changes with predictable consequences. Harnessing this idea, we herein create a range of anisotropically grown bimetallic NPs to order. The power of this approach is then demonstrated through the use of these designed nanomaterials as highly efficient ORR electrocatalysts.

2. Results and Discussion

2.1. Nanoparticle Synthesis

The strategy above recently provided proof-of-concept for the independent control of morphology and composition in Pt/Fe NPs specifically.^[14] We now harness the far-reaching implications of this to create a range of Pt/M (M = Ni, Co) systems by making systematic changes to synthetic conditions to either render the system gradually more reducing or to selectively limit or promote the inclusion of the different metals in Pt/M. While doing this we also sought to ensure a versatile, rapid, and potentially scalable approach based on facile conditions and accessible reagents. To achieve this, we used a simple one-pot synthesis that works under normal pressure and modest temperatures (250–300 °C) in a short time (30 min). Mixtures of the commercially available salts Pt(acac)₂ and M(acac)₂ (acac = acetylacetonate) are treated with a combination of OA and OAm, followed by strong reductant 1,2-hexadecanediol (1,2-HDD) to promote complete reduction of metal ions to Pt⁰ and M⁰. The tractable, commercially accessible combination of the liquids OA and OAm offers a range of ben-

efits in bimetallic NP formation. Its action has been the subject of review,^[29] with a mixture of carboxyl anions, protonated oleylamine, and acid-base complexes generated depending on conditions; electron donation by the carboxyl anions offering particular stabilization to NPs during growth.^[30] Meanwhile, ligand exchange and the in situ formation of metal oleates provide further leverage to modulate how strongly reducing the system is.^[31] Moreover, in contrast to the action of OA as a capping agent, OAm is established to be both a capping and reducing agent, enabling it to promote reduction, particularly at elevated temperatures.^[14] Concerning anisotropic growth, OA/OAm modulates the relative growth between the (111) and (100) facets of Pt/M^[32] since OAm preferentially binds to the (100) facet (cube face). This accelerates growth on the (111) facet (cube corners) of a cuboctahedral seed, yielding anisotropic growth. At the same time, OA is a facet-indiscriminate capping agent, favoring symmetric cuboctahedra. This behavior has been further evidenced by Pt/Fe nanocube formation following the sequential addition of OA and OAm, with OA first allowing the overgrowth of the (100) cube face.^[33] By harnessing the points outlined above, we seek dual control over composition and morphology by balancing the rate of reduction in each system studied here with the rate of kinetic NP growth. Practically, we do this by 1) Achieving kinetic growth by adjusting the reduction rate, initially by manipulating the OA:OAm ratio whilst maintaining a constant total volume; 2) Expanding the kinetic growth regime by varying absolute OAm level to alter metal salt concentration and how reducing the system is; 3) Fine-tuning reducing conditions using temperature to either increase (higher temperature) or decrease (lower temperature) reduction rate; 4) Defining a new kinetic growth regime as necessary by raising or lowering the level of one metal salt used to selectively vary the contribution of that metal in the product. To the best of our knowledge, this understanding of the effects had by systematically manipulating variables in points 1–4 yields the first set of overarching principles for systematically creating bimetallic, anisotropic NPs in which both composition and morphology vary predictably. Results are summarised in **Figure 2** and **Table 1**. Detailed structure and composition data and a full explanation of the relationship between synthetic conditions and product characteristics for each sample are in Electronic Supporting Information (ESI) sections **2.1** and **2.2**. The main observations are summarized below.

Work to identify the kinetic growth regime (point 1) in Pt/Ni synthesis is shown in **Figure S1** (Supporting Information). The observed mixture of pseudospherical seeds and small NPs achieved using a 1.4:0.6 OA:OAm ratio (vol:vol) suggests mainly thermodynamic growth. The proportion of OAm has therefore been increased, with the hoped for formation of nanopods becoming almost ubiquitous in **Figure S3** (Supporting Information) (1:1 OA:OAm), where EDX mapping suggests intermixed Pt and Ni. The critical concentration of nanopods recently established to trigger nanodendrite formation in Pt/Fe systems^[14] can be achieved here by using yet more strongly reducing conditions (0.5:1.5 OA:OAm; **Figure S5**, Supporting Information). We have next sought to move the nanopod concentration beyond that suitable for forming nanodendrites (point 2, above). Accordingly, while adding 0.5 mL OAm still gives nanodendrites (**Figure S6**, Supporting Information), adding *another* 0.5 mL OAm (0.5:2.5 OA:OAm) gives a mixture of nanodendrites, nanopods,

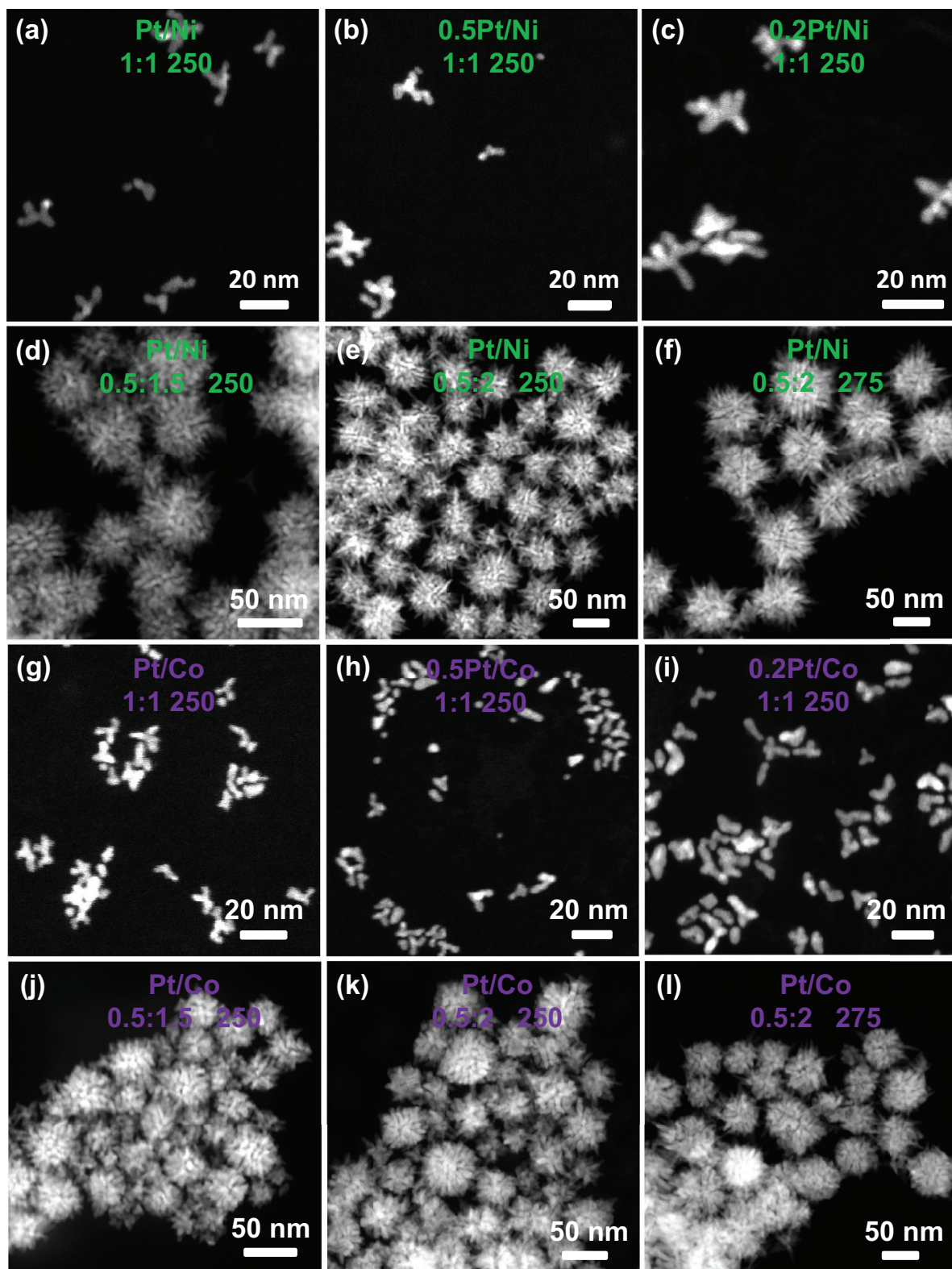


Figure 2. High-angle annular dark field (HAADF) imaging summary of Pt-deficient, equimolar, and Pt-rich NPs. Nanopodal Pt/Ni (a)-(c), Pt/Co (g)-(i), and nanodendritic Pt/Ni (d)-(f), Pt/Co (j)-(l) are prepared as described in Table 1. Each figure shows the OA:OAm ratio and temperature ($^{\circ}\text{C}$) used in the synthesis. Reactions employed a 1:1 ratio of metal substrates unless otherwise stated (0.5:1 in (b,h), 0.2:1 in (c,i)).

Table 1. Syntheses and compositions of samples shown in Figure 2. Scanning transmission electron microscopy-energy dispersive X-ray spectroscopy (STEM-EDX) data represent mean and standard deviation for 10 randomly selected regions and independent corroboration comes from inductively-coupled plasma-optical emission spectroscopy (ICP-OES).

Pt/M	Figure 2	Sample	Protocol ^{a)}	EDX [At% Pt]	ICP-OES [At% Pt]
Pt/Ni	(a)	Pt-rich, nanopod	1:1, 1:1, 250	65.2 ± 4.9	70.9
	(b)	Equimolar, nanopod	0.5:1, 1:1, 250	50.5 ± 6.6	58.8
	(c)	Pt-poor, nanopod	0.2:1, 1:1, 250	42.5 ± 4.2	50.7
	(d)	Pt-rich, nanodendrite	1:1, 0.5:1.5, 250	64.3 ± 1.8	64.1
	(e)	Equimolar, nanodendrite	1:1, 0.5:2, 250	56.5 ± 1.8	58.0
	(f)	Pt-poor, nanodendrite	1:1, 0.5:2, 275	43.6 ± 3.5	51.9
Pt/Co	(g)	Pt-rich, nanopod	1:1, 1:1, 250	72.1 ± 9.2	71.6
	(h)	Equimolar, nanopod	0.5:1, 1:1, 250	62.2 ± 8.3	59.6
	(i)	Pt-poor, nanopod	0.2:1, 1:1, 250	42.4 ± 5.7	55.5
	(j)	Pt-rich, nanodendrite	1:1, 0.5:1.5, 250	62.2 ± 9.4	71.3
	(k)	Equimolar, nanodendrite	1:1, 0.5:2, 250	50.2 ± 6.6	58.1
	(l)	Pt-poor, nanodendrite	1:1, 0.5:2, 275	41.6 ± 10.8	51.7

^{a)} Pt:M reagents (ratio by moles), OA:OAm (ratio by mL), Temp. (°C).

near-pseudospheres, and large nanoobjects (Figure S7, Supporting Information). EDX mapping suggests this last morphology is based on Ni. Moving to the study of temperature (point 3 above), an OA:OAm ratio of 0.5:2 has been used, and on raising the temperature from 250 °C to 300 °C, a similar transition from nanodendrites to a mixture of morphologies occurs (Figure S9, Supporting Information). Lastly, concerning point 4 above, Figure S13 (Supporting Information) shows that nanodendrites can be made with specific compositions (Pt-rich, equimolar, Pt-poor) using equimolar metal reagents. Meanwhile, Pt-rich (65 At% Pt, Figure S3, Supporting Information) and equimolar (48 At% Pt, Figure S2, Supporting Information) Pt/Ni nanopods are achieved by a similar approach. Lowering the level of Pt reagent in the reaction (0.2:1 Pt:Ni, Figure S15, Supporting Information) can then be used to achieve Pt-poor nanopods whilst achieving an obvious cost saving.

The generality of our approach allows it to be extended to Pt/Co. When varying OA:OAm at constant total volume, data are similar to those observed for Pt/Ni (Figures S16–S19, Supporting Information) with near-pseudospheres under low-OAm conditions transitioning to compositionally intermixed, polycrystalline nanopods and then ≈50 nm nanodendrites as the proportion of OAm is raised at the expense of OA, reaction volume is increased using OAm, or temperature is raised. However, in a point of contrast, whereas the strongly reducing OA:OAm = 0.5:2.5 system gives large, randomly-shaped Ni nanoobjects in Pt/Ni experiments, similar Pt/Co work instead results in the ≈50 nm nanodendrites being added to by larger (≈90 nm) nanodendrites (Figure S23, Supporting Information). Lastly, Figure S13 (Supporting Information) summarizes how Pt/Co nanodendrites can be prepared at specific compositions (Pt-rich, equimolar, Pt-poor) using equimolar metal combinations. Once more, this approach also accesses Pt-rich nanopods (72 At% Pt, Figure S17c, Supporting Information). Attempts to retain morphology whilst lowering the Pt contribution in the product by using more Co reagent failed (see Supporting Information). Instead, lowering the Pt precursor level to one-half and then one-fifth that of Co gives

nanopods with progressively lower Pt contributions of 62 At% (Figure S24c, Supporting Information) and 42 At% (Figure S25c, Supporting Information), respectively, whilst achieving a significant economic saving. Clearly, a cost-effective strategy emerges here for varying Pt composition within morphologically defined NPs. Taken together with the facile conditions and quick, one-pot nature of preparative work, results point to a versatile, scalable approach to anisotropic catalysts.

Lastly, powder X-ray diffraction (PXRD) analysis (Figures S29 and S30, Supporting Information) confirms the expected formation of both Pt⁰ and M⁰ through the appearance of lattice fringes corresponding to the known 111 and 200 planes of previously reported fcc Pt/M (M = Ni, Co).^[13,34,35] Notably, the ORR activity of Pt/Ni varies according to the trend (100) < (110) < (111).^[36] This being so, having proved the broad applicability of our strategy for achieving simultaneous yet independent control over composition and morphology, we have sought to verify product utility in ORR.

2.2. Oxygen Reduction Electrocatalysis

The design principles outlined above offer for the first time a wide-ranging solution to a currently unmet need. That is, for preparing simple and more efficient Pt-based electrocatalysts through *systematic* control during the synthesis of anisotropic bimetallics. This, in turn, will promote the use of ultralow catalyst loading, which has dual benefits. First, there are obvious cost and energy security implications. Second, it reduces the risk of particle agglomeration on the electrode surface. The efficacy of our approach is tested here through ORR experiments in 1 M KOH,^[37,38] which provides a point of reference to our related work in the field^[9] (for comparative data obtained using 0.1 M KOH see Supporting Information). Moreover, this selection of conditions feeds into our wider interests in sustainability in the context of developing technologies that boast anti-corrosion credentials. In the current case, ORR chemistry is well established

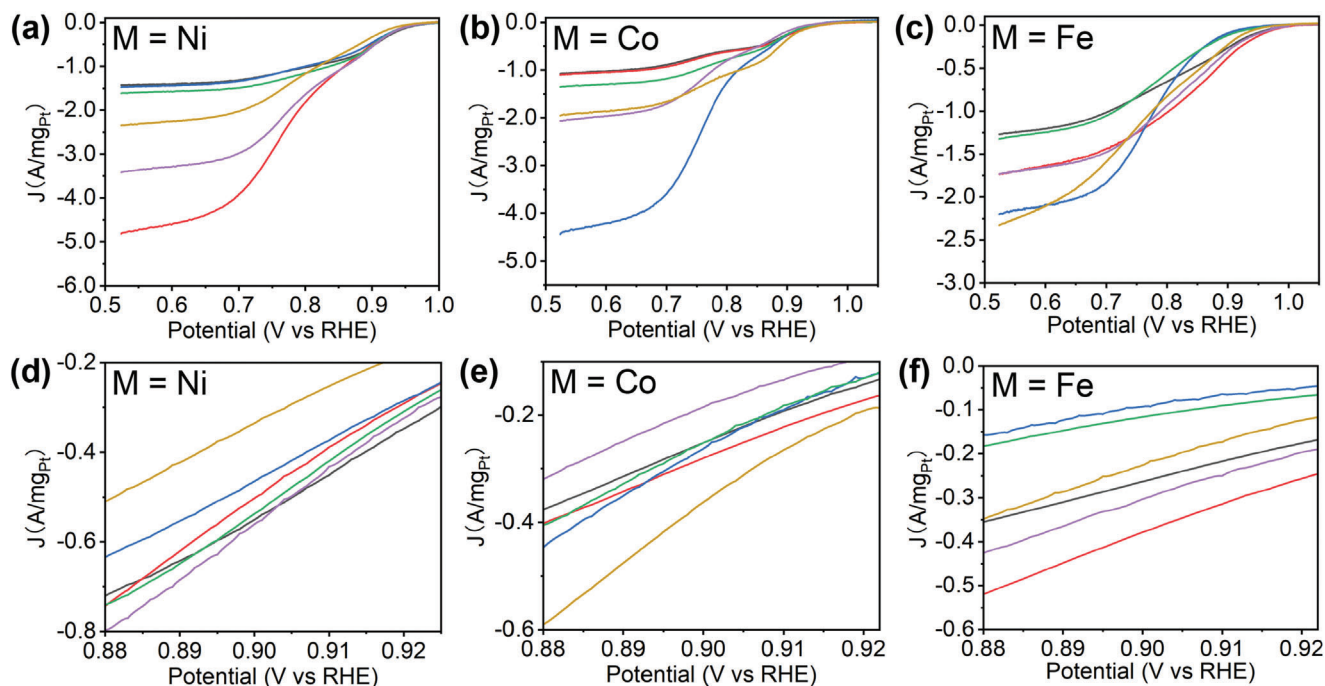


Figure 3. a–c) Average mass activity-potential curves for anisotropic Pt/M catalysts based on 3 independent thin-film electrodes in O₂ saturated 1 M KOH (pH 14) with a scan rate of 20 mV s⁻¹. — Pt-rich nanodendrite, — equimolar nanodendrite, — Pt-poor nanodendrite, — Pt-rich nanopod, — equimolar nanopod, — Pt-poor nanopod. d–f) Expansions of (a)–(c) respectively focusing on E = 0.9 V versus RHE.

as proceeding by 2e⁻ or 4e⁻ reduction.^[39] In acidic media, the 2e⁻ pathway sequentially generates (corrosive) peroxide.^[40] Our use of basic conditions avoids this, with 2e⁻ reduction giving HO₂⁻ and both 2e⁻ and 4e⁻ pathways generating OH⁻.^[41] Having now systematically prepared a range of differently composed and structurally anisotropic ORR candidates, initial measurements use Pt-rich, equimolar, and Pt-poor nanopods and nanodendrites of recently reported Pt/Fe (for exact compositions see Figure 5g in ref. [14]) as well as currently reported Pt/M (M = Co, Ni; for exact compositions see Table 1 in this work). Measurements utilize a three-electrode setup in aqueous KOH under saturated oxygen conditions at room temperature. Notably, in recent studies, novel Pt-alloy electrocatalysts have exhibited ORR activities approaching those expected at the oxygen diffusion limit.^[42] To mitigate the potential errors that accompany ORR activity so high that the raw kinetic currents associated with it approach oxygen diffusion limited currents, we use extremely low catalyst loadings (0.5 μg_{Catalyst} per disk). The resulting ORR mass activity curves for the potentials 0.5–1.05 V versus reversible hydrogen electrode (RHE, for conversion of data from Ag/AgCl (saturated NaCl) reference electrode see ESI) are shown in Figure 3 (for mass activity curves see Figures S31–S36 (Supporting Information), for current densities see Figure S37 (Supporting Information), and for data on 10 wt% (0.68 At%) Pt/C standard see Figure S38, Supporting Information). Results underscore the significant influence on ORR performance of controlling both NP shape and composition by making simple changes to the conditions under which they are synthesized.

The very low catalyst loadings deployed in this work led us to focus our interest on the kinetic regimes in Figure 3.^[38] This analysis, customarily undertaken at 0.9 V versus RHE,^[43] allows

the most promising samples to be selected from each Pt/M series and not only their mass activity (A/mg_{Pt}), but their current density (mA cm⁻²), onset potential (V), half-wave potential (V) and diffusion-limited current density (mA cm⁻²) to be compared. For Pt/Ni, 2 systems produce near identical high-mass activities (Figure 3a,d); Pt-rich nanodendrites and equimolar nanopods. Of these, the former yields not only more reproducible potential curves (Figures S31 and S32, Supporting Information) but also a considerably enhanced current density (1.21 vs 0.44 mA cm⁻², Figure S37d, Supporting Information). Pt-rich nanodendrites are therefore focused on below. These data point to the ability of the many-armed structure of the nanodendrite sample to express a higher surface area, logically exposing more surface Pt for ORR activity. A similar message comes from the Pt/Fe data, where equimolar nanodendrites clearly yield the most compelling specific and mass activities (Figures S35 and S37f, Supporting Information). The situation for Pt/Co is more complicated. While Figure S37e (Supporting Information) reveals similar current density for 4 samples, the best-performing system (equimolar nanodendrites) exhibits a relatively flat polarization curve. Analysis of mass activity then shows that, of these 4 samples, Pt-poor nanopods exhibit superior behavior. This observation highlights 2 points. First, normalizing activity for the mass of Pt means that low-Pt samples may be catalytically competitive even if their intrinsic activity is lower. Second, and in contrast to the other 2 systems, Pt/Co nanopods exhibit the best activity. We correlate this with the unusually dense, compact appearance of the Pt/Co nanodendrites, which we argue limits reagent access to surface Pt. This contrasts with the less complex (more active) nanodendrites seen for both Ni and Fe.^[14] We consider that for Pt/Co, nanopods offer greater reagent access to surface Pt active sites.

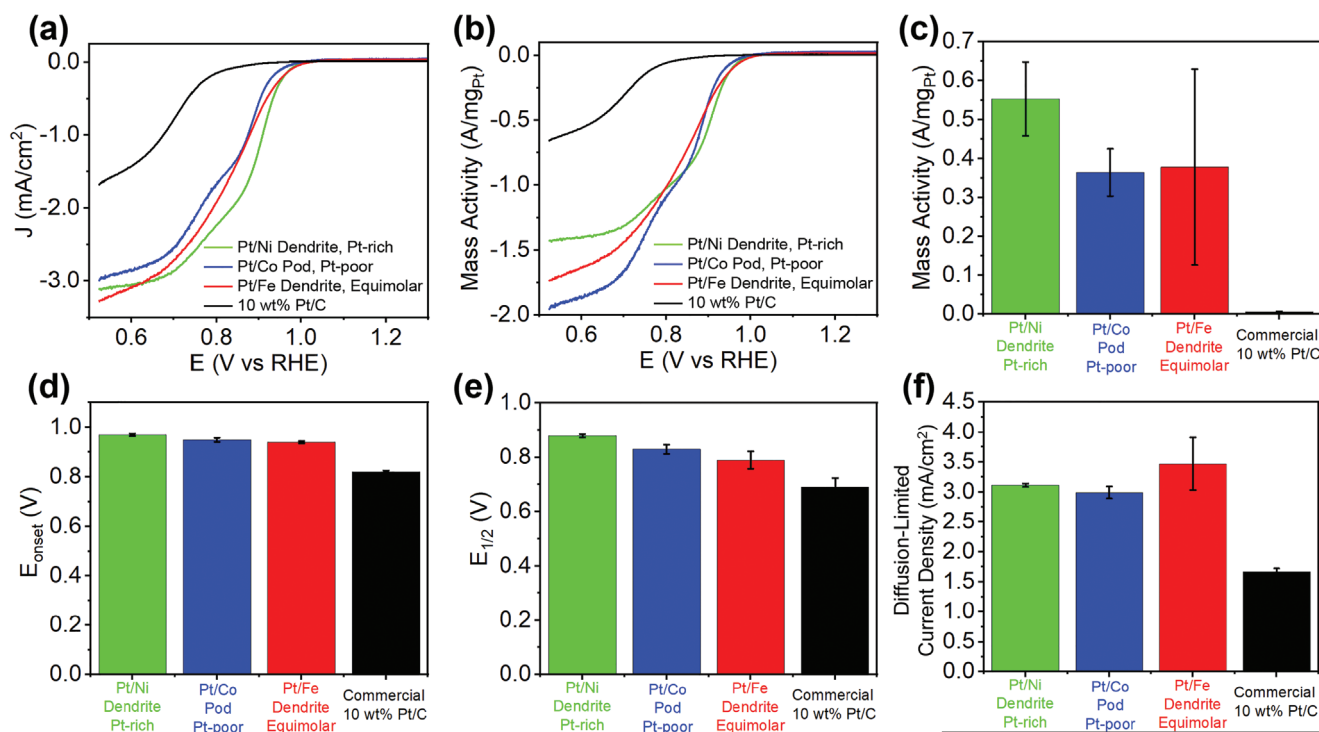


Figure 4. a) ORR polarization curves for the best-performing example of each system illustrated in Figure 3 and 10 wt% Pt/C standard; b) corresponding plot of mass activity; summaries of c) mass activity at 0.9 V versus RHE, d) E_{onset} , e) $E_{1/2}$, and f) diffusion-limited current density for each sample. For ORR conditions, see Figure 3 legend.

ORR polarization curves and corresponding mass activities of the 3 samples identified as most promising from the preliminary analysis above – Pt-rich Pt/Ni nanodendrites, Pt-poor Pt/Co nanopods, and equimolar Pt/Fe nanodendrites – are shown in Figure 4 and compared to those of industry standard 10 wt% Pt/C NPs. All 3 significantly outperform the reference in terms of both current density and mass activity. This is attributed to their anisotropic structures rendering more surface Pt available for reaction. Notably, the current densities (Figure 4a) correlate with composition; Pt-rich Pt/Ni > equimolar Pt/Fe > Pt-poor Pt/Co. Meanwhile, in spite of mass activity being normalized for Pt content, Pt/Co still performs worst (Figure 4b,c), and this is attributed to its nanopodal rather than nanodendritic structure. Our 3 anisotropic samples exhibit very similar onset potentials (E_{onset}), with that of Pt-rich Pt/Ni nanodendrites being marginally best at 0.97 V versus RHE (these nanodendrites also significantly outperform equimolar Pt/Ni nanopods for E_{onset} , see above). Notably, all 3 samples show substantially more positive E_{onset} than the reference (Figure 4d; Figures S37 and S39, Supporting Information). Since E_{onset} is the potential at which the current density reaches 0.1 mA cm⁻², the need for a lower potential to promote ORR is taken to reflect our anisotropic systems offering more surface active sites than the standard. Though our E_{onset} values are excellent,^[44] the unusually poor performance of the standard speaks to the errors that can manifest when studying highly active ORR catalysts where raw currents must be lowered by using reduced catalyst loadings.^[42] We address this by analyzing the potential at which half the limiting diffusion current is achieved (half-wave potential, $E_{1/2}$). At 0.88 V versus RHE

(Figure 4e), nanodendritic Pt-rich Pt/Ni yields the highest $E_{1/2}$, emphasizing the benefit of achieving a specific current density at a lower overpotential.^[45] The diffusion-limited current densities seen in this work are as expected for the ultralow Pt loadings studied.^[38] Those of all 3 samples lie within error and, at 3.11 mA cm⁻², that of Pt-rich Pt/Ni nanodendrites is nearly twice the 1.67 mA cm⁻² returned by commercial 10 wt% Pt/C NPs (Figure 4f), offering the potential for increased power when applied in a fuel cell. Lastly, an initial assessment of the stability of our nanodendritic Pt-rich Pt/Ni relative to that of the reference is undertaken (Figures S40 and S41, Supporting Information) with results showing an initial drop in activity, which we attribute to the aerial oxidation of Ni.^[46,47] It is notable that, while a decline in activity is seen, the nanodendrites maintain their superior activity with respect to the Pt/C reference. So far as we are aware, stability measurements on comparable catalysts reported in the literature (see below and Table S1, Supporting Information) have not hitherto been established at loadings that approach the ultralow ones we employ here. These systems are expected to be influenced by large errors, with even very small amounts of metal leaching likely to affect activity to a high degree.

Considering the data above, the optimal catalyst in this work is Pt-rich nanodendritic Pt/Ni, which achieves a mass activity of 0.55 A mg_{Pt}⁻¹ and current density of 1.21 mA cm⁻² at 0.9 V versus RHE using an ultralow Pt loading of 0.0022 mg_{Pt} cm⁻². This surpasses the 10 wt% Pt/C reference sample by 87 and 75 times in terms of mass activity and current density, respectively (Figure 4c; Figure S39a, Supporting Information). The high ratio of mass activity between our best-performing catalyst and that of Pt/C

standard provides a convenient point of comparison with the prior art. Relevant literature is cited in Table S1 (Supporting Information). While our own work in which Pt/Fe octopods were incorporated in Pt/Fe-Fe₃O₄ nanodumbbells deployed a comparable ultralow catalyst loading, in that case, the mass activity ratio of the dumbbell to standard was just 3.2:1 (Table S1, entry 1, Supporting Information).^[9] Moving to the most competitive mass activity normalized for Pt, even highly engineered mesoporous frameworks have yielded a mass activity ratio of 29:1 with respect to Pt/C, and then using a Pt loading 3 times greater than that in this work (Table S1, entry 11, Supporting Information).^[2] Other recent studies suffer from a range of issues. While combining multiple precious metals (Table S1, entry 5, Supporting Information)^[48] has cost implications, most require the engineering of heterostructures (Table S1, entries 6, 9, 10, Supporting Information)^[3,49,50] and/or specific compositions (Table S1, entry 8, Supporting Information).^[51] In the most recent work to appear, thermal annealing or high-temperature chemical vapour deposition (Table S1, entries 12, 13, Supporting Information),^[22,52] or the multistep immobilization of Pt/Fe on carbons (Table S1, entries 14, 15, Supporting Information)^[23,53] or MXene (Table S1, entry 16, Supporting Information)^[54] introduce complexity and restrict scalability. Avoiding these drawbacks, a simple ultrasonication approach to Pt/Ni on carbon has been reported that reinforced the importance of compositional control in bimetallic catalysts, though a high loading (40 wt%) of Pt-rich (83 At%) NPs was required (Table S1, entry 17, Supporting Information).^[55] Interesting work on holey, ultrathin nanosheets of Pt₃M yielded Pt₃Ni under mild conditions but required 6 h heating. In terms of mass activity, this performed 10 times better than Pt/C at a catalyst loading of 20.4 μg_{Pt} cm⁻² (Table S1, entry 18, Supporting Information).^[56] Of other prior art that reports intermixed Pt/Ni NPs, aging was required to achieve a concave-faceted, Pt-rich architecture (Table S1, entry 7, Supporting Information). This catalyst outperformed the standard by 27 times but required a high 255 μg_{Catalyst} cm⁻² loading.^[57] Meanwhile, a general approach to Pt/M nanopods has been suggested previously (Table S1, entries 2–4, Supporting Information),^[13] though those systems deployed 51 μg_{Catalyst} cm⁻² and delivered mass activities 3.3–5.3 times that of Pt/C reference.^[13] Lastly, semimetal intermetallic compounds of Pt, though without morphological or compositional variability, have recently emerged as ORR candidates, outperforming Pt/C by 6 times for Pt/Sb (Table S1, entry 19, Supporting Information).^[24]

3. Conclusion

This work has demonstrated a pathway toward the creation of cost-efficient Pt-based catalysts, both the compositions and morphologies of which can be independently manipulated. Unlocking this strategy has achieved 2 significant goals. First, precise control over both chemical makeup and anisotropy in a range of heterobimetallic nanopods and nanodendrites. Second, a streamlined, 1-pot synthesis (solvent-free, 250 °C, 30 min) that uses relatively affordable, easily handled reagents. The different compositions and morphologies that result have been tested for ORR activity and all significantly outperform commercial 10 wt% Pt/C. It is possible to interpret trends in both mass activity and current density; correlating them with composition and structure,

respectively, and this makes clear the benefits of being able to systematically vary both. Meanwhile, compelling E_{onset} and E_{1/2} can be rationalized in terms of active site availability. In the case of best-performing Pt-rich nanodendritic Pt/Ni, an ultralow catalyst loading of 0.0022 mg_{Pt} cm⁻² lowers costs and reduces the risk of particle agglomeration, returning an onset potential of 0.97 V versus RHE compared with one of 0.82 V versus RHE for Pt/C, with mass activity and current density values surpassing those of the reference by more than 87 and 75 times, respectively. The clear performance enhancement available through this level of synthetic control at the nanoscale points to a new phase in the development of affordable noble metal-based catalysts. Having established the generality of our synthetic approach and its ability to furnish highly active systems, efforts are now being directed toward 1) investigating catalyst lifecycles at ultralow loadings, and 2) understanding the atomistic nature of the active sites. For point 1, repeat cycling tests already evidence preconditioning effects and the emergence of a trend for catalyst performance plateauing. Future lifecycle tests are expected to confirm this and will underpin an investigation of whether catalysts undergo restructuring or agglomeration. Concerning this, the potential of extended nanodendritic structures for resisting close-packing and for offering very high surface area-volume ratios with scope for chemical functionalization (either inducing electrostatic repulsion between NPs or anchoring them to the electrode surface)^[58] will be explored. These ideas feed into point 2, where spectroscopic and high-resolution transmission electron microscopic studies on as-prepared and spent electrode surfaces and material recovered from them will underpin DFT interrogation not only of surface features and compositions but also of their evolution.

Supporting Information

Supporting Information is available from the Wiley Online Library or from the author.

Acknowledgements

S.M. thanks CSC Cambridge for a scholarship. S.J.C. thanks the Leverhulme Trust for an Early Career Fellowship (ECF-2021-072), the Isaac Newton Trust (20.08(r)), and Darwin College, Cambridge for financial support. M.R. acknowledges the European Commission for a Horizon 2020 Marie Skłodowska-Curie Individual European Fellowship (SolarFUEL, GAN 839763). N.S. thanks Jesus College, Cambridge for a Sheldrick Scholarship. The EPSRC is also acknowledged for supporting electron microscopy at Cambridge (Underpinning Multi-User Equipment; EP/P030467/1). Ariffin Bin Mohamad Annuar is thanked for help with the PXRD analysis.

Conflict of Interest

The authors confirm there are no conflicts of interest.

Data Availability Statement

Material supporting this study is supplied as Electronic Supporting Information and Open Data are available at <http://doi.org/10.17863/CAM.104244>. The authors have also applied a Creative Commons Attribution (CC BY) license to any Author Accepted Manuscript version arising.

Keywords

anisotropic catalyst, bimetallic catalyst, nanodendrite, oxygen reduction reaction, platinum

Received: June 23, 2024

Revised: July 16, 2024

Published online:

- [1] Z. Ma, Z. P. Cano, A. Yu, Z. Chen, G. Jiang, X. Fu, L. Yang, T. Wu, Z. Bai, J. Lu, *Angew. Chem., Int. Ed.* **2020**, *132*, 18490.
- [2] H. Jin, Z. Xu, Z. Y. Hu, Z. Yin, Z. Wang, Z. Deng, P. Wei, S. Feng, S. Dong, J. Liu, S. Luo, Z. Qiu, L. Zhou, L. Mai, B. L. Su, D. Zhao, Y. Liu, *Nat. Commun.* **2023**, *14*, 1518.
- [3] Z. Zhao, Z. Liu, A. Zhang, X. Yan, W. Xue, B. Peng, H. L. Xin, X. Pan, X. Duan, Y. Huang, *Nat. Nanotechnol.* **2022**, *17*, 968.
- [4] F. Xiao, Q. Wang, G. L. Xu, X. Qin, I. Hwang, C. J. Sun, M. Liu, W. Hua, H. wen Wu, S. Zhu, J. C. Li, J. G. Wang, Y. Zhu, D. Wu, Z. Wei, M. Gu, K. Amine, M. Shao, *Nat. Catal.* **2022**, *5*, 503.
- [5] M. Luo, Z. Zhao, Y. Zhang, Y. Sun, Y. Xing, F. Lv, Y. Yang, X. Zhang, S. Hwang, Y. Qin, J. Y. Ma, F. Lin, D. Su, G. Lu, S. Guo, *Nature* **2019**, *574*, 81.
- [6] X. Ge, A. Sumboja, D. Wu, T. An, B. Li, F. W. T. Goh, T. S. A. Hor, Y. Zong, Z. Liu, *ACS Catal.* **2015**, *5*, 4643.
- [7] S. Cao, T. Sun, J. R. Li, Q. Z. Li, C. C. Hou, Q. Sun, *Nano Res.* **2023**, *16*, 4365.
- [8] B. Lim, Y. Xia, *Angew. Chem., Int. Ed.* **2011**, *50*, 776.
- [9] K. J. Jenkinson, A. Wagner, N. Kornienko, E. Reisner, A. E. H. Wheatley, *Adv. Funct. Mater.* **2020**, *30*, 2002633.
- [10] S. Cheong, J. D. Watt, R. D. Tilley, *Nanoscale* **2010**, *2*, 2045.
- [11] X. Song, S. Luo, X. Fan, M. Tang, X. Zhao, W. Chen, Q. Yang, Z. Quan, *Front. Chem.* **2018**, *6*, 468.
- [12] G. M. Leteba, G. M. Leteba, D. R. G. Mitchell, P. B. J. Levecque, L. Macheli, E. Van Steen, C. I. Lang, *ACS Appl. Nano. Mater.* **2020**, *3*, 5718.
- [13] W. Lei, M. Li, L. He, X. Meng, Z. Mu, Y. Yu, F. M. Ross, W. Yang, *Nano Res.* **2020**, *13*, 638.
- [14] S. Ming, A. E. H. Wheatley, *Nanoscale* **2023**, *15*, 8814.
- [15] B. W. Zhang, H. L. Yang, Y. X. Wang, S. X. Dou, H. K. Liu, *Adv. Energy Mater.* **2018**, *8*, 1703597.
- [16] C. Wei, S. Sun, D. Mandler, X. Wang, S. Z. Qiao, Z. J. Xu, *Chem. Soc. Rev.* **2019**, *48*, 2518.
- [17] L. Huang, Y. Han, S. Dong, *Chem. Comm.* **2016**, *52*, 8659.
- [18] M. U. Khan, L. Wang, Z. Liu, Z. Gao, S. Wang, H. Li, W. Zhang, M. Wang, Z. Wang, C. Ma, J. Zeng, *Angew. Chem., Int. Ed.* **2016**, *55*, 9548.
- [19] X. Wang, Z. Li, Y. Qu, T. Yuan, W. Wang, Y. Wu, Y. Li, *Chem* **2019**, *5*, 1486.
- [20] J. K. Nørskov, J. Rossmeisl, A. Logadottir, L. Lindqvist, J. R. Kitchin, T. Bligaard, H. Jónsson, *J. Phys. Chem. B.* **2004**, *108*, 17886.
- [21] V. R. Stamenkovic, B. Fowler, B. S. Mun, G. Wang, P. N. Ross, C. A. Lucas, N. M. Markovic, *Science* **2007**, *315*, 493.
- [22] X. Zhao, B. Hui, X. Chen, T. Jia, X. Yu, L. Li, X. Zhang, Z. Lu, X. Yang, *Appl. Surf. Sci.* **2024**, *663*, 160183.
- [23] S. Shin, E. Lee, J. Nam, J. Kwon, Y. Choi, B. J. Kim, H. C. Ham, H. Lee, *Adv. Energy Mater.* **2024**, 2400599.
- [24] H. Cheng, R. Gui, C. Chen, S. Liu, X. Cao, Y. Yin, R. Ma, W. Wang, T. Zhou, X. Zheng, W. Chu, Y. Xie, C. Wu, *Nat. Sci. Rev.* **2024**, nwa233.
- [25] S. Sharma, C. Zeng, A. A. Peterson, *Catal. Sci. Technol.* **2024**, <https://doi.org/10.1039/d4cy00463a>.
- [26] T. H. Yang, Y. Shi, A. Janssen, Y. Xia, *Angew. Chem., Int. Ed.* **2020**, *59*, 15378.
- [27] Y. Wang, J. He, C. Liu, W. H. Chong, H. Chen, *Angew. Chem., Int. Ed.* **2015**, *54*, 2022.
- [28] R. Chen, Q. N. Nguyen, Y. Xia, *ChemNanoMat* **2022**, *8*, 202100474.
- [29] S. Mourdikoudis, M. Menelaou, N. Fiuza-Maneiro, G. Zheng, S. Wei, J. Pérez-Juste, L. Polavarapu, Z. Sofer, *Nanoscale Horiz.* **2022**, *7*, 941.
- [30] V. Patsula, E. Petrovsky, J. Kovářová, R. Konefal, D. Horák, *Colloid Polym. Sci.* **2014**, *292*, 2097.
- [31] X. Guo, W. Wang, Y. Yang, Q. Tian, *CrystEngComm* **2016**, *18*, 9033.
- [32] S. W. Chou, C. L. Zhu, S. Neeleshwar, C. L. Chen, Y. Y. Chem, C. C. Chen, *Chem. Mater.* **2009**, *21*, 4955.
- [33] M. Chen, J. Kim, J. P. Liu, H. Fan, S. Sun, *J. Am. Chem. Soc.* **2006**, *128*, 7132.
- [34] S. Sun, C. B. Murray, D. Weller, L. Folks, A. Moser, *Science* **2000**, *287*, 1989.
- [35] Y. Yu, W. Yang, X. Sun, W. Zhu, X. Z. Li, D. J. Sellmyer, S. Sun, *Nano Lett.* **2014**, *14*, 2778.
- [36] Y. J. Wang, N. Zhao, B. Fang, H. Li, X. T. Bi, H. Wang, *Chem. Rev.* **2015**, *115*, 3433.
- [37] W. Y. Yan, S. L. Zheng, W. Jin, Z. Peng, S. N. Wang, H. Du, Y. Zhang, *J. Electroanal. Chem.* **2015**, *741*, 100.
- [38] G. Zhong, S. Xu, L. Liu, C. Z. Zheng, J. Dou, F. Wang, X. Fu, W. Liao, H. Wang, *ChemElectroChem* **2020**, *7*, 1107.
- [39] R. Ma, G. Lin, Y. Zhou, Q. Liu, T. Zhang, G. Shan, M. Yang, J. Wang, *NPJ Comput. Mater.* **2019**, *5*, 78.
- [40] N. Kornienko, J. Z. Zhang, K. P. Sokol, S. Lamaison, A. Fantuzzi, R. Van Grondelle, A. W. Rutherford, E. Reisner, *J. Am. Chem. Soc.* **2018**, *140*, 17923.
- [41] C. Wan, X. Duan, Y. Huang, *Adv. Energy Mater.* **2020**, *10*, 1903815.
- [42] S. S. Kocha, K. Shinozaki, J. W. Zack, D. J. Myers, N. N. Kariuki, T. Nowicki, V. Stamenkovic, Y. Kang, D. Li, D. Papageorgopoulos, *Electrocatalysis* **2017**, *8*, 366.
- [43] Y. Garsany, O. A. Baturina, K. E. Swider-Lyons, S. S. Kocha, *Anal. Chem.* **2010**, *82*, 6321.
- [44] W. Chen, J. Huang, J. Wei, D. Zhou, J. Cai, Z. Da He, Y. X. Chen, *Electrochem. Commun.* **2018**, *96*, 71.
- [45] J. Wang, C. X. Zhao, J. N. Liu, D. Ren, B. Q. Li, J. Q. Huang, Q. Zhang, *Nano Mater. Sci.* **2021**, *3*, 313.
- [46] E. S. Lambers, C. N. Dykstal, J. M. Sen, J. L. Rowe, P. H. Holloway, *Oxid. Met.* **1996**, *45*, 301.
- [47] S. Liu, J. Zong, Z.-J. Zhao, J. Gong, *Green Chem. Eng.* **2020**, *1*, 56.
- [48] X. Peng, D. Lu, Y. Qin, M. Li, Y. Guo, S. Guo, *ACS Appl. Mater. Interfaces* **2020**, *12*, 30336.
- [49] P. Weber, D. J. Weber, C. Dosche, M. Oezaslan, *ACS Catal.* **2022**, *12*, 6394.
- [50] G. M. Leteba, D. R. Mitchell, P. B. Levecque, E. Van Steen, C. I. Lang, *RSC Adv.* **2020**, *10*, 29268.
- [51] H. Ding, P. Wang, C. Su, H. Liu, X. Tai, N. Zhang, H. Lv, Y. Lin, W. Chu, X. Wu, C. Wu, *Adv. Mater.* **2022**, *34*, 2109188.
- [52] J. He, C. Chen, H. Yu, Y. Zhao, M. Xu, T. Xiong, Q. Lu, Z. Yu, K. Tai, J. Tan, C. Liu, *J. Mater. Sci. Technol.* **2025**, *212*, 139.
- [53] Y. Dong, P. Song, C. Han, W. Xu, *J. Electroanal. Chem.* **2024**, *959*, 118189.
- [54] Y. Zhang, Q. Zhao, B. Danil, W. Xiao, X. Yang, *Adv. Mater.* **2024**, *36*, 2400198.
- [55] R. K. Polagani, P. L. Suryawanshi, M. Chinthala, S. H. K. Annamareddy, N. Nasani, S. H. Sonawane, *Asia-Pac. J. Chem. Eng.* **2024**, *19*, e2993.
- [56] H. C. Kim, R. K. Pramadewandaru, M. K. Kabiraz, G. A. Bin Azizar, H. Wahidah, Y. Kim, S.-U. Lee, H.-J. Chae, S.-I. Choi, J. W. Hong, *ACS Catal.* **2024**, *14*, 3756.
- [57] G. M. Leteba, Y. C. Wang, T. J. Slater, R. Cai, C. Byrne, C. P. Race, D. R. Mitchell, P. B. Levecque, N. P. Young, S. M. Holmes, A. Walton, *Nano Lett.* **2021**, *21*, 3989.
- [58] S.-N. Hu, W.-C. Xu, N. Tian, S.-M. Chen, M.-Y. Li, J.-F. Shen, J.-X. Lin, S.-L. Guo, X.-Y. Huang, Z.-Y. Zhou, S.-G. Sun, *Energy Environ. Sci.* **2024**, *17*, 3099.